Li-Doped Cr_2MnO_4: A New p-Type Transparent Conducting Oxide by Computational Materials Design

Haowei Peng, Andriy Zakutayev, Stephan Lany, Tula R. Paudel, Mayeul d'Avezac, Paul F. Ndione, John D. Perkins, David S. Ginley, Arpun R. Nagaraja, Nicola H. Perry, Thomas O. Mason, and Alex Zunger*

To accelerate the design and discovery of novel functional materials, here, p-type transparent conducting oxides, an inverse design approach is formulated, integrating three steps: i) articulating the target properties and selecting an initial pool of candidates based on "design principles", ii) screening this initial pool by calculating the "selection metrics" for each member, and iii) laboratory realization and more-detailed theoretical validation of the remaining "best-of-class" materials. Following a design principle that suggests using d5^5 cations for good p-type conductivity in oxides, the Inverse Design approach is applied to the class of ternary Mn(II) oxides, which are usually considered to be insulating materials. As a result, Cr_2MnO_4 is identified as an oxide closely following "selection metrics" of thermodynamic stability, wide-gap, p-type dopability, and band-conduction mechanism for holes (no hole self-trapping). Lacking an intrinsic hole-producing acceptor defect, Li is further identified as a suitable dopant. Bulk synthesis of Li-doped Cr_2MnO_4 exhibits at least five orders of magnitude enhancement of the hole conductivity compared to undoped samples. This novel approach of stating functionality first, then theoretically searching for candidates that merits synthesis and characterization, promises to replace the more traditional nonsystematic approach for the discovery of advanced functional materials.

1. Introduction: Inverse Design of New Functional Materials

Advanced materials with new functionalities often require a combination of several materials properties that are counter-indicated and difficult to achieve simultaneously. Transparent conducting oxides (TCOs), particularly the p-type variety, are an example of such materials, requiring simultaneously optical transparency and p-type (hole-carrier) electrical conductivity. Although p-type transparent conducting oxides (TCOs) are desirable in many optoelectronic applications,[1] such materials are much more difficult to design and make compared to their n-type counterparts. The difficulties arise from the generally heavier effective masses of holes compared to electrons, the tendency for self-compensation of p-type doping in oxides, and the frequent occurrence of small-polarons that impede effective hole conduction. Indeed, the basic principles controlling p-type conductivity in wide-gap materials have yet to be established beyond heuristics, so the rational design has thus far been difficult. This is reflected, in part, by numerous attempts at p-type doping of ZnO, which has created intense interest and research activity, but still remains a matter of ongoing debate.[2]

Here we apply the inverse design approach to searching for p-type TCOs, which was proposed to address the inverse problem in materials science that can be formulated as: given the target properties, find the material (chemical space search) or configuration (structure search) that has this property. Inverse design is an approach powered by theory guiding experiment, and three modalities have been developed for different types of search problems. Modality 1 of inverse design is the inverse band-structure (IBS) method,[3] which applies to cases[3,4] when one needs to figure out the specific atomic configuration of a fixed chemical system having the target properties. This can be done by combining a configurational search, such as genetic algorithms and simulated annealing, with quantum mechanical calculations of the target properties. In Modality 2 of inverse design, considered in this paper, the search is directed to the chemical space consisting of known compounds with currently unknown properties (such as the ≈10^5 compounds documented in the inorganic crystal structure database (ICSD)).[5] Often, the desired functionality requires a non-trivial combination of several target properties, for example, good optical transparency, high charge carrier mobility and concentration for a TCO, or high figure of merit

---

Dr. H. Peng, Dr. A. Zakutayev, Dr. S. Lany,
Dr. T. R. Paudel, Dr. M. d'Avezac, Dr. P. F. Ndione,
Dr. J. D. Perkins, Dr. D. S. Ginley
National Renewable Energy Laboratory
15013 Denver West Parkway, Golden, CO 80401, USA
E-mail: Haowei.Peng@nrel.gov
A. R. Nagaraja, Dr. N. H. Perry, Prof. T. O. Mason
Department of Materials Science and Engineering
Northwestern University
Evanston, IL 60208, USA
Prof. A. Zunger
University of Colorado
Boulder, CO 80309, USA

DOI: 10.1002/adfm.201300807

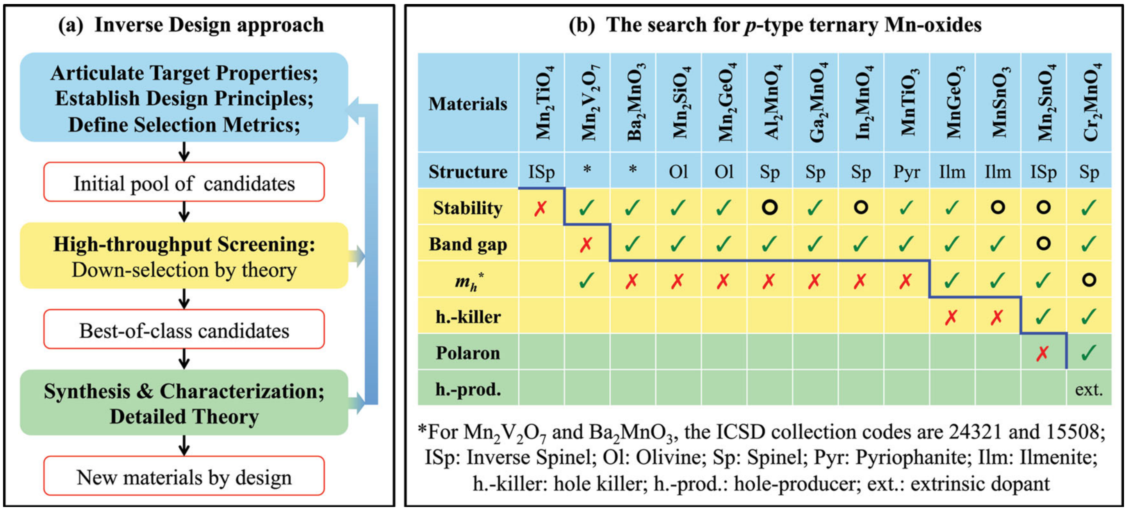

Materials	Mn_2TiO_4	$Mn_2V_2O_7$	Ba_2MnO_3	Mn_2SiO_4	Mn_2GeO_4	Al_2MnO_4	Ga_2MnO_4	In_2MnO_4	$MnTiO_3$	$MnGeO_3$	$MnSnO_3$	Mn_2SnO_4	Cr_2MnO_4
Structure	ISp	*	*	Ol	Ol	Sp	Sp	Sp	Pyr	Ilm	Ilm	ISp	Sp
Stability	✗	✓	✓	✓	✓	○	✓	○	✓	✓	○	○	✓
Band gap		✗	✓	✓	✓	✓	✓	✓	✓	✓	✓	○	✓
m_h^*		✓	✗	✗	✗	✗	✗	✗	✗	✓	✓	✓	○
h.-killer										✗	✗	✓	✓
Polaron												✗	✓
h.-prod.													ext.

*For $Mn_2V_2O_7$ and Ba_2MnO_3, the ICSD collection codes are 24321 and 15508; ISp: Inverse Spinel; Ol: Olivine; Sp: Spinel; Pyr: Pyriophanite; Ilm: Ilmenite; h.-killer: hole killer; h.-prod.: hole-producer; ext.: extrinsic dopant

Figure 1. a) Flowchart diagram illustrating the inverse design approach; b) a check mark indicates that the respective materials property is suitable for the desired functionality of a p-type TCO, a circle indicates a non-optimal, but still acceptable value for this property, and a cross mark indicates that this property is prohibitive. The line (blue) indicates the sequential down-selection. In Cr_2MnO_4, extrinsic dopants (ext.) are needed for the presence of acceptor-like hole-producers.

ZT for a thermoelectric material. In order to screen promising materials from a larger chemical space, we established a set of selection metrics (sometimes called "descriptors") that are properties reflecting crucial aspects of the target properties, but unlike the latter are readily calculable using modern first principles techniques. Examples of p-type TCO metrics include band gaps, hole effective masses and polaron, hole-producing and -killing defects, and so forth. Such metrics are used to downselect the most promising materials from the initial pool, and to focus experimental and subsequent theoretical studies on this narrow set of best-of-class candidates. The basic procedure of Modality 2 inverse design incorporates three steps, as illustrated in the color-coded flow-chart, **Figure 1**a. This modality has recently been employed for searching for p-type TCOs[6,7] and photovoltaic (PV) absorber materials,[8] with a combined theoretical and experimental approach. In Modality 3 inverse design, the subject is the search for new compounds that are not documented in databases like the ICSD. Here, high-throughput energy minimization and thermodynamic stability analysis are needed to identify the ground-state crystal structure and stability of many material systems, each with many possible structures and configurations.[9,10] Newly discovered stable compounds from Modality 3 are subsequently included in the functionality-driven screening of Modality 2.

Given a large number (≈100 000) of known compounds in the ICSD, it is desirable to pre-select, prior to the application of computational selection metrics and experimental studies, a narrower class of materials within which the target properties are likely to occur. Historically, such choices were done by heuristic rules of thumb, or by ingenious (or lucky) guesses. These rules of thumb could be a priori rules obtained from past experience in solid-state chemistry, or rules distilled later on as an outcome of the current research. We will refer to either case as design principles, which are primarily used to define the initial class of materials that are to be subjected to the selection metrics. While the traditional selection of an initial pool for p-type TCOs has been d^{10} oxides (such as $CuAlO_2$, Ag_3VO_4)[6,11] or d^6 oxides (Rh_2ZnO_4),[12] our initial pool consists of d^5 ternary Mn-oxides, that have previously not been considered as promising materials for TCO applications. In fact, they were viewed as insulators in the past, and have not been deemed promising for optical transparency owing to possible d–d multiplet transitions.[13] Specifically, for Cr_2MnO_4, the room temperature conductivities of undoped samples have been reported from 10^{-11} to 10^{-13} S cm^{-1},[14,15] and the optical properties are largely unknown except for the dielectric constant (perhaps due to the lack of interest).[14] By contrast, our inverse design approach arrives at Li-doped Cr_2MnO_4 as a new p-type transparent compound with conductivity of 1.1×10^{-2} S cm^{-1} that may be capable of further improvement by epitaxial thin film or single crystal growth.

2. Target Properties, Design Principles, and Selection Metrics for p-type TCOs (Step 1; Blue)

2.1. Target Properties

The basic target properties we aim for *p*-type TCOs include a high degree of optical transparency in the visible range, as well as a high hole mobility and concentration.

2.2. Design Principles and Selection of Initial Pool of Candidates: Mn(II)-Based Oxides

In this study, we have selected an initial pool of candidates consisting of the Mn(II)-based ternary oxides, directed by the d^5-design principle that utilizes transition-metal cations with a high-spin d^5 configuration. According to our recent study of the prototypical d^5 oxides MnO and Fe_2O_3,[16] p–d coupling in these d^5 materials is similar to the case of the d^{10} configuration of

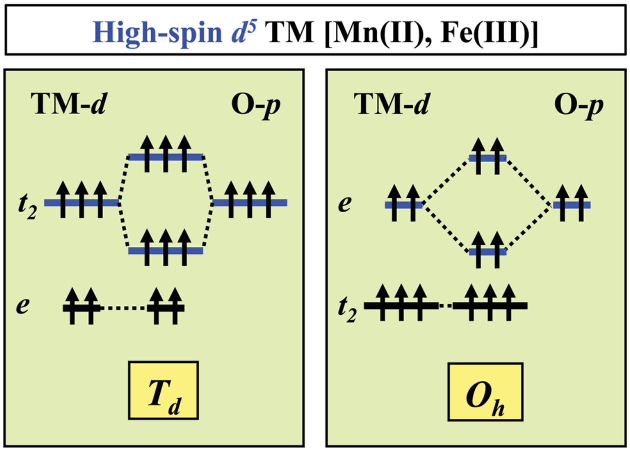

Figure 2. The schematic diagram for the p–d coupling in compounds where the transition-metal cation with a high-spin d^5 configuration, like Mn(II) and Fe(III), is tetrahedrally (Td) or octahedrally (Oh) coordinated.

Cu(I) (e.g., in $CuAlO_2$)[11] and Ag(I) (e.g., in Ag_3VO_4),[6] except that the interaction with the ligands occurs mostly in the occupied spin channel. In **Figure 2**, we illustrate the p–d coupling for compounds containing high-spin Mn(II) or Fe(III) cations. In such materials, the VBM will be the anti-bonding state, formed between the cation *d*-state and the oxygen *p*-state with the same symmetry. This p–d repulsion increases the valence band dispersion, and hence is expected to result in a lighter hole effective mass:[11,17] the anti-bonding (light-mass) state is t_2 for tetrahedral and e for octahedral coordination environments, whereas the non-bonding (heavier-mass) is e for tetrahedral and t_2 for octahedral. At the same time, this p–d repulsion raises the energy level of the valence band maximum (VBM) (being now closer to vacuum), which is expected to enhance the p-type dopability.[11,18] Furthermore, in the high-spin d^5 configuration of Mn(II), the large exchange splitting allows a large band-gap, and the internal d–d transitions are spin-forbidden, which supports acceptable transparencies in sufficiently thin films.

While the introduction of such *d*-states is instrumental for p-type conductivity, it also potentially induces electronic correlation effects that can lead to undesired carrier localization and self-trapping (small-polaron formation),[16,19] as discussed for $CuAlO_2$.[20] We paid special attention to such effects in the present study.

During the initial selection, compounds containing V(III), V(IV), Ti(III), Mn(III), Fe(III), and Cu(II) ions were excluded, since their band-gaps would be significantly limited by the unoccupied *d*-states lying relatively low in energy. For example, the empty *d*-states are only about 2 eV above the O-*p*-like VBM in Fe_2O_3 (6 eV in MnO), even with the presence of strong exchange splitting.[16] Thus, the initial pool of candidates consists of 13 compounds from the ICSD, which are $Mn_2V_2O_4$ with the ICSD collection code 24321 (ICSD 24321), $Ba_2Mn_2O_3$ with the ICSD collection code 15508 (ICSD 15508), Mn_2TiO_4, and Mn_2SnO_4 with the inverse spinel (ISp) structure, Al_2MnO_4, Ga_2MnO_4, In_2MnO_4, and Cr_2MnO_4 with the spinel (Sp) structure, Mn_2SiO_4 and Mn_2GeO_4 with the olivine (Ol) structure, $MnTiO_3$, $MnGeO_3$, and $MnSnO_3$ with the ilmenite (Ilm) structure ($MnTiO_3$ is labeled with its own mineral name Pyrophanite (Pyr)).

2.3. Defining Calculable Selection Metrics for Screening the Initial Pool

We use six metrics to down-select *p*-TCOs from the initial list:

M-1: Thermodynamic stability. The compound should be stable against decomposition under experimentally accessible synthesis/growth conditions. Since in Modality 2 used here the compounds are selected from a database of previously made compounds, overall stability is generally assured. This metric determines however the minimum (O-poor, reducing) and maximum (O-rich, oxidizing) oxygen chemical potentials of the stability range, from which we can infer whether a compound requires particular oxidizing or reducing conditions to be stable.

M-2: A sufficiently wide band-gap, ideally above 3 eV for transparency, or at least a sufficiently low absorption coefficient to allow acceptable transparency of a thin film typically on the order of 100 nm thick.

The target property of good hole mobility is represented by metrics M-3 and M-4:

M-3: Light hole effective mass. Generally, the mobility is inversely proportional to the effective mass. While hole masses in oxides are generally larger ($m_h*/m_e > 1$) than in conventional semiconductors, a not-too-heavy effective hole mass is needed to support good p-type conductivity.

M-4: Hole self-trapping should not happen, so as to avoid the undesirable small-polaron transport mechanism.[12,19] In order to distinguish between a band and a small-polaron conduction mechanism for holes,[12,19] we need to calculate the energy difference between the self-trapped polaronic hole state and the band-like hole state at the VBM, that is, the self-trapping energy E_{ST}, for hole polarons. A negative E_{ST} indicates an undesired small-polaron conduction mechanism, while a positive E_{ST} indicates a desired band conduction mechanism.

The target property of sufficient free hole concentrations, which can be assessed by defect calculations,[21] is embodied in metrics M-5 and M-6:

M-5: Absence of spontaneously formed hole-killer defects, that is, intrinsic defects that act as positively charged compensating donors, for example, O vacancies (V_O^{2+}) or cation interstitials, or antisite donors involving high-valent cations on low-valent sites.[22–24] Such hole-killer defects create a positively charged donor state, which compensates p-type carriers.[22] To practically calculate the propensity of a material to develop such hole-killer defects we note that the formation energy ΔH_D of such hole-killer defects decreases when the Fermi level E_F approaches the VBM. When ΔH_D approaches zero, E_F reaches its pinning level for p-type doping, $E_F^{p,\mathrm{pin}}$.[24] We will calculate $E_F^{p,\mathrm{pin}}$ and determine if it lies deep inside the band gap (in which case the material is not p-type dopable, because hole doping is countered by self-compensation).[25]

M-6: The presence of spontaneously formed hole-producer defects. A good hole-producing defect or dopant should have low formation energy so as to form in sufficient concentrations, and should have small acceptor ionization energy so that free carriers are excited thermally at room temperature. The oxides considered here are all insulators when perfect, and holes will be created by certain defects, either intrinsic defects like cation vacancies, antisite donors involving low-valent cations on high-valent sites, etc., or extrinsic p-type dopants. We have previously proposed four doping types (DT) in semiconductors based on their intrinsic defect properties.[26] Denoting the transition energy level[21] of the dominant hole-killers (donors) as ε_D, that of the dominant hole-producers (acceptors) as ε_A, and the energy of the VBM and conduction band minimum (CBM) of the parent semiconductor as E_V and E_C, respectively: DT-1 to -4 correspond to the cases of $\varepsilon_D > \varepsilon_A$, $\varepsilon_A > E_V > \varepsilon_D$, $\varepsilon_A > E_C > \varepsilon_D$, and $E_C > \varepsilon_A > \varepsilon_D > E_V$, respectively. In DT-1, the system could be p-type without extrinsic doping if ε_A is close enough to the VBM and the formation energy of the hole-killers are high enough. Systems in DT-2 and DT-3 are readily p- and n-type without extrinsic doping. In DT-4, the system is insulating until extrinsic p- or n-type impurities are added through doping. The best case for *p*-TCO is DT-1 followed by DT-4.

3. Screening by High Throughput First-Principles Calculations (Step 2; Yellow)

In this step, we narrowed the initial pool of material candidates down to the "best-of-class", employing high-throughput computation of a subset of metrics for these candidates. The thermodynamic stability (M-1), electronic structure properties, including quasi-particle band-gap and optical absorption coefficient (M-2) and hole effective mass (M-3), and intrinsic defect properties (M-5 and M-6) were evaluated in this step. The tendency of forming small-polaron (M-4), and extrinsic doping (M-6) will be considered for the "best-of-class" materials as detailed theory in the next step.

All calculations were performed using the plane-wave density functional theory method with the formalism of the projector-augmented waves (PAW),[27] as implemented in the Vienna Ab-initio Simulation Package (VASP).[28] For the thermodynamic stability, the hole effective masses, and defect calculations, we used the generalized gradient approximation (GGA) as parameterized elsewhere[29] for the exchange-correlation functional. A moderate on-site U[30] of 3.0 eV is applied for *d* orbitals in 3*d* transition metals. In the supercell calculations, finite-sized effects have been corrected.[21] For the calculation of the compound formation energy and the thermodynamic stability, we used the fitted elemental reference energies.[31] Based on this type of GGA+U calculation, we performed subsequent band-structure calculations in the GW approximation.[32]

3.1. Thermodynamic Stability of Parent Compounds (M-1)

In order to evaluate the thermodynamic stability, we calculated the compound formation enthalpies (enthalpy relative to the elements), and determined the relative stability versus that of other binary or ternary phases. This analysis ("triangular analysis")[9,10] yields the range of elemental chemical potentials under which the ternary compound is thermodynamically stable.

Among the 13 compounds, only the inverse spinel Mn_2TiO_4 is unstable, showing an exothermic heat of reaction for decomposition into MnO and pyrophanite $MnTiO_3$. For the other 12 compounds, **Table 1** gives the minimum (O-poor, reducing) and maximum (O-rich, oxidizing) oxygen chemical potentials of the stability range, from which we can infer whether a compound requires particular oxidizing or reducing conditions to be stable. In order to put the numerical values for the chemical potentials into context, we determined from ideal gas law calculations,[33] $\Delta\mu_O = -0.7$ eV for an exemplary oxidizing condition corresponding to $pO_2 = 1$ atm at $T = 673$ K (400 °C), and

Table 1. For the Mn-containing ternary oxides of interest, the calculated heat of formation ΔH_f, oxygen chemical potentials $\Delta\mu_O$ and competing phases at the O-poor/reducing and O-rich/oxidizing limits, quasi-particle band gaps E_g, optical absorption threshold E_{abs}, and hole effective masses m_h*. For the structure, the mineral name is used when available, otherwise the ICSD collection code is given.

Compound	ΔH_f [eV]	$\Delta\mu_O$ [eV]		Competing phases		E_g [eV]	E_{abs} [eV]	m_h* [m_e]
		O-poor	O-rich	O-poor	O-rich			
$Mn_2V_2O_7$ (ICSD 24321)	–25.8	–1.8	–0.4	Mn_2O_3; MnV_2O_6	Mn_3O_4; VO_2	0.6	0.7	0.8
Ba_2MnO_3 (ICSD 15508)	–15.8	–4.4	–1.4	MnO; BaO	Mn_3O_4; BaO	2.9	2.9	16.7
Mn_2SiO_4 (olivine)	–17.7	–4.2	–1.7	MnO; SiO_2	Mn_3O_4; SiO_2	5.3	5.9	14.2
Mn_2GeO_4 (olivine)	–14.5	–3.2	–1.7	MnO; $MnGeO_3$	Mn_3O_4; $MnGeO_3$	4.0	4.4	18.5
Mn_2SnO_4 (inverse spinel)	–14.0	–2.8	–1.9	MnO; SnO	Mn_3O_4; SnO_2, $MnSnO_3$	2.2	2.7	3.4
Al_2MnO_4 (spinel)	–21.5	–4.2	–1.8	MnO; Al_2O_3	Mn_3O_4; Al_2O_3	6.0	6.1	12.4
Ga_2MnO_4 (spinel)	–15.6	–3.5	–1.4	MnO; Ga_2O_3	Mn_3O_4; Ga_2O_3	4.2	4.2	19.3
In_2MnO_4 (spinel)	–13.6	–3.2	–2.5	MnO; In_2O_3	Mn_3O_4; In_2O_3	3.0	3.1	21.3
Cr_2MnO_4 (spinel)	–16.4	–4.1	–0.8	MnO; Cr_2O_3	Mn_2O_3, Mn_3O_4; Cr_2O_3	3.3	3.5	9.8
$MnTiO_3$ (pyrophanite)	–14.1	–4.0	–1.3	MnO; TiO_2	Mn_3O_4; TiO_2	3.8	3.8	14.4
$MnGeO_3$ (ilmenite)	–10.2	–2.9	–1.4	Mn_2GeO_4, GeO_2	Mn_2GeO_4, Mn_3O_4; GeO_2	4.4	3.8	5.9
$MnSnO_3$ (ilmenite)	–9.8	–2.6	–1.9	Mn_2SnO_4; SnO, SnO_2	Mn_3O_4, Mn_2SnO_4; SnO_2	3.2	3.4	3.0

$\Delta\mu_O = -3.2$ eV for a reducing condition corresponding to $pO_2 = 10^{-10}$ atm at $T = 1473$ K (1200 °C). In Table 1, we also give the competing compounds that determine the boundaries of phase stability under the O-poor (reducing) and O-rich (oxidizing) conditions, which define the boundaries in the phase diagram. For example, for Cr_2MnO_4, MnO and Cr_2O_3 are the competing phases that accommodate Mn- and Cr-excess, respectively, under reducing conditions (note that metallic phases may also occur under very reducing conditions).

Except Mn_2TiO_4, all other ternary Mn-oxides studied here were found to be stable under specific conditions. (Note that Mn_2TiO_4 could still exist as a metastable phase, or due to stabilization because of entropy effects at higher temperatures.) We observe, however, that many Mn(II) oxides, like Mn_2SnO_4, $MnSnO_3$, and In_2MnO_4, require rather reducing conditions, which can make the experimental synthesis difficult. This consideration is taken into account in the stability criterion in Figure 1b, where $\Delta\mu_O > -1.8$ eV under the oxidizing condition (Table 1) was included as a desirable property, so as to allow synthesis at an experimentally reasonable temperature and pO_2 ($\Delta\mu_O = -1.8$ eV corresponds to $pO_2 = 10^{-3}$ atm at 1000 °C).

3.2. Electronic Structure Properties: Band-Gap and Optical Absorption (M-2), and Hole Effective Mass (M-3)

The quasi-particle band-gaps and inter-band optical absorption spectra are calculated within the GW approximation (*G* is the one-particle Green's function, and *W* is the dynamically screened Coulomb potential), where the initial GGA+U wavefunctions are kept fixed, but the eigenenergies are iterated to self-consistency. Density-functional-derived local-field effects[34] have been taken into account. In the case of Cr oxides, GW is found to place the *d*-states too high in energy, hence overestimating the band gap of Cr_2O_3, similar to the case of TiO_2.[6,35] An on-site potential[24] $V_d = -3.5$ eV for Cr-*d* is used to correct the band gap of Cr_2O_3 of about $E_g = 3.2$ eV,[36,37] and this parameter is also used to predict the gap of Cr_2MnO_4. For the effective masses, the density-of-states effective mass[6] was calculated, instead of the band curvature effective mass, due to the non-parabolic valence band structure of the considered materials. In order to obtain converged effective masses for $T = 300$ K, we used a very dense *k*-point sampling in the Brillouin-zone within GGA+U, using at least 20 000/number of atoms *k*-points.[38]

Table 1 gives the calculated band gaps, and the threshold energy for absorption due to direct inter-band optical transitions. The absorption threshold is defined as the photon energy at which the calculated absorption coefficient α becomes larger than 10^2 cm^{-1} (α is calculated in the independent particle approximation, without excitonic effects, internal *d-d* transition, and phonon- or disorder-induced indirect or forbidden transitions considered). $Mn_2V_2O_7$ is found to have a small quasi-particle band gap of only 0.6 eV with a slightly indirect band gap, so we will exclude this material from further investigation. Mn_2SnO_4 has a relatively small quasi-particle band gap of 2.21 eV, however significant optical absorption does not occur until 2.7 eV. The other compounds have both band gaps and optical absorption thresholds larger than 3.1 eV, indicative of excellent optical transparency in the visible spectrum.

As for the hole effective mass, the underlying idea of the design principle was that the Mn–d^5 shell interacts with the O–*p* states and thereby increases the valence band dispersion. Observing the overlap between the Mn–*d* and O–*p* density of states (DOS), we confirmed that the p–d coupling occurs in all compounds. However, in compounds with the olivine and spinel structure, the hole effective mass is still quite high, as shown in Table 1. The relatively high effective mass in spinel Ga_2MnO_4, In_2MnO_4, and Cr_2MnO_4 is probably due to the lack of a geometrically connected network of Mn-tetrahedra. (For conventional n-type TCO's, it is found that the conductivity is approximately in proportion to the density of the electron-carrying cation-centered octahedra.)[39] But in Cr_2MnO_4, we found some contribution from Cr–*d* to the DOS at the VBM despite their nominal non-bonding t_2 character, which results in a better effective mass. Based on this metric, we screened out Ba_2MnO_3, Mn_2SiO_4, Mn_2GeO_4, Al_2MnO_4, Ga_2MnO_4, In_2MnO_4, and $MnTiO_3$ from further consideration, as shown in Figure 1b.

3.3. Intrinsic Defect Properties: Absence of Hole-Killers (M-5), and Presence of Hole-Producers (M-6)

Using high-throughput defect calculations,[26] we determined the position of the p-type pinning level $E_F{}^{p,\mathrm{pin}}$ in $MnGeO_3$, $MnSnO_3$, Mn_2SnO_4, and Cr_2MnO_4. Comparing with Cr_2MnO_4, we also calculated the intrinsic defect properties for Ga_2MnO_4 and In_2MnO_4. The defect formation energies and transition energy levels were calculated.[21] We found that the pinning level lies inside the band gap within the entire stability range (see Table 1) of $MnGeO_3$, $MnSnO_3$, Ga_2MnO_4, and In_2MnO_4, suggesting that hole-killer defects (Ge_{Mn}, Sn_{Mn}, Ga_{Mn}, and In_{Mn}, respectively) spontaneously form in these compounds and therefore intrinsically limit the hole carrier concentrations. Mn_2SnO_4 and Cr_2MnO_4 pass this selection metric. In **Figure 3**a,b, we show the calculated $E_F{}^{p,\mathrm{pin}}$ as a function of the oxygen chemical potential under both the Mn-poor and Mn-rich conditions. In Mn_2SnO_4, $E_F{}^{p,\mathrm{pin}}$ determined by the Sn_{Mn} antisite defect lies below the VBM under all growth conditions (Figure 3b), implying the absence of self-compensation. In Cr_2MnO_4, under the Mn-poor, and Mn-rich O-rich condition, Cr_{Mn} determines $E_F{}^{p,\mathrm{pin}}$, while under the Mn-rich and O-poor (reducing) condition, V_O determines $E_F{}^{p,\mathrm{pin}}$. As shown in Figure 3b, $E_F{}^{p,\mathrm{pin}}$ lies below the VBM under most growth conditions.

In Figure 3a,b, we also plotted the defect transition energy levels, which correspond to the thermal ionization energies, for the dominant native donor and acceptor defects. According to that classification of doping types proposed recently for A_2BO_4 spinel oxides,[26] Mn_2SnO_4 and Cr_2MnO_4 belong to the DT-1 and DT-4 doping types, respectively. Due to the rather shallow (0/1-) acceptor level and the low $E_F{}^{p,\mathrm{pin}}$, a preliminary conclusion from the screening step (Figure 1) is that Mn_2SnO_4 could be p-type if the sample was prepared under the Mn-rich condition. By contrast, Mn and Cr in Cr_2MnO_4 tend to form charge-neutral defects when forming anti-site defects, by exchanging their oxidation state. This behavior implies that the intrinsic acceptor is not electrically active, that is, even though Cr_2MnO_4 is p-type dopable, it requires extrinsic dopants to achieve actual p-type conductivity that will be investigated in the next step.

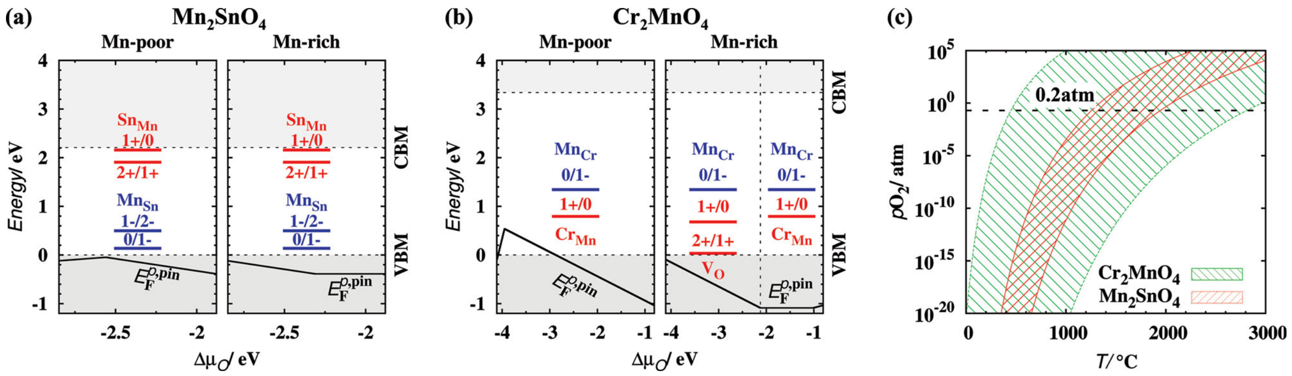

Figure 3. Properties of the "best-of-class" materials Mn_2SnO_4 and Cr_2MnO_4: a) the calculated p-type pinning Fermi level ($E_F^{p,pin}$) for Mn_2SnO_4 as a function of the oxygen chemical potential ($\Delta\mu_O$) under both the Mn-poor (Sn/Cr-rich) and Mn-rich (Sn/Cr-poor) conditions, and the transition energy levels for the dominant native donor (red) and acceptor (blue) defects; b) the same as (a) but for Cr_2MnO_4; c) the stability range for $\Delta\mu_O$ (Table 1), shown as a (pO_2 vs. T) diagram.

4. Targeted Synthesis and Characterization and Detailed Theory (Step 3; Green)

After the high-throughput screening step, inverse spinel Mn_2SnO_4 and spinel Cr_2MnO_4 are the two remaining "best-of-class" materials, which were then subject to in-depth experimental and theoretical study in the third step of the inverse design approach (see Figure 1). In step 3 of Modality 2 inverse design, we concentrate on experimental synthesis and characterization of bulk and thin film samples, as well as more specialized, in-depth theoretical investigations of the final best-of-class material.

4.1. Experimental Synthesis

Bulk samples of Cr_2MnO_4 and Mn_2SnO_4 were synthesized by solid-state sintering. For Cr_2MnO_4, stoichiometric amounts of dried Cr_2O_3 (99.97% purity) and MnO_2 (99.997% purity, Alfa Aesar, Ward Hill, MA) were ground together with a mortar and pestle under acetone. Pellets approximately 12.5 mm in diameter were uniaxially pressed at ≈130 MPa, surrounded by sacrificial powder of the same composition, and placed in nested crucibles. The samples were then fired at 1473 K (1200 °C) for 12 h and quenched to room temperature in air. These synthesis condition is well within the predicted stability range depicted in Figure 3c, which was obtained by expressing the limiting oxygen chemical potentials of Table 1 as a pO_2 versus T diagram by means of the ideal gas law behavior of $\Delta\mu_O(pO_2, T)$.[33]

For Mn_2SnO_4, stoichiometric amounts of dried MnO (99.99%, Alfa Aesar) and SnO_2 (≥99.99%, Sigma-Aldrich, St. Louis, MO) were ground together and pressed, as described for Cr_2MnO_4. The pellets were nested inside a bed of sacrificial powder of identical composition in an alumina boat and sintered in an atmosphere-controlled tube furnace ($pO_2 \approx 7 \times 10^{-15}$atm using H_2/H_2O mixtures at 1200 °C) for 10 h. The samples were cooled at 5–10 °C min^{-1} to room temperature in this same gas mixture. This synthesis condition accounts for the fact that Mn_2SnO_4 requires more reducing conditions than Cr_2MnO_4 (Figure 3c). (Note that for the nominal T, pO_2 values, one would ultimately expect further reduction of Sn(IV) to Sn(II) in SnO, but the spinel formation from the binary oxides is the dominating process for the present experimental variables.) Pellet surfaces were ground off prior to electrical and optical characterization.

The crystal structures of these samples were confirmed by X-ray diffraction. The Cr_2MnO_4 sample contained approximately 1 wt% Cr_2O_3 secondary phase, but the majority of the sample was the desired spinel phase. We do not expect that the minor secondary phase significantly affected the electrical or optical measurements. The Mn_2SnO_4 sample appeared to be single-phase spinel, although it is possible that it contained trace amounts of MnO, given that the X-ray diffraction peaks of the two phases overlap.

Thin films of Cr_2MnO_4 (230 nm) and Mn_2SnO_4 (500 nm) were prepared using radio frequency co-sputtering from MnO and Cr_2O_3 or SnO_2 targets. The targets were pointed at a 45° angle to glass substrates heated to 400–800 °C in the case of Cr_2MnO_4 and to 400 °C in the case of Mn_2SnO_4. All depositions were performed in 2×10^{-5} atm of Ar atmosphere in a vacuum chamber with 2×10^{-9} atm H_2O base pressure (estimated pO_2 during the deposition is 2×10^{-9} atm). Both composition and thickness of these samples was determined using X-ray fluorescence (XRF) measurements. The crystal structure of these samples was determined using X-ray diffraction (XRD).

4.2. Measured Optical Properties and Comparison with Theory

For bulk samples, we measured diffuse reflectance spectra using a PerkinElmer LAMBDA 1050 UV/Vis/NIR spectrophotometer equipped with a 150 mm Integrating Sphere accessory (PerkinElmer, Waltham, MA). A standard Kubelka-Munk analysis was performed.[37,40] For the thin-films, we measured the specular transmittance and reflectance using a fiber optics-based Oceanoptics spectrometer with normal incident angle of light. The spectrometer is equipped with mercury and halogen light sources and grating-based CCD detectors. The absorption coefficient α was determined from transmittance Tr and reflectance R using the $\alpha = -\ln[Tr/(1-R)]/d$ relationship, where d is

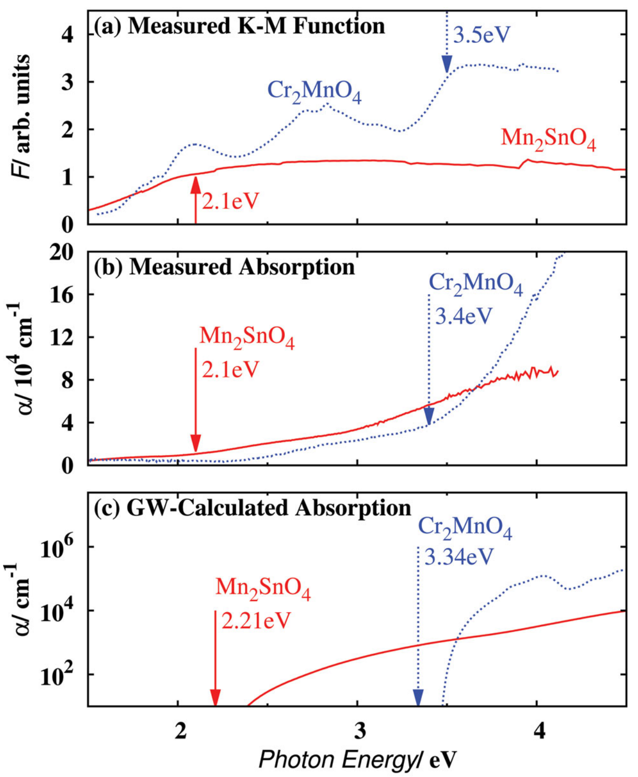

Figure 4. a) The Kubelka-Munk function F from diffuse reflectance measurement on bulk pellet samples, b) the absorption spectrum from specular transmittance and reflectance measurement on thin-film samples, and c) calculated GW absorption for Mn_2SnO_4 (red, solid) and Cr_2MnO_4 (blue, dashed). The optical band gaps in (a) and (b), and the calculated fundamental band gaps in (c) are denoted by arrows.

the thickness of the thin film. This analysis removes from the absorption spectra the effects of oscillations present in transmittance and reflectance spectra due to interference of light between the front and backsides of the film. The calculated absorption spectrum was determined in the independent particle approximation from the GW quasi-particle energy spectrum (see above).

The results for the optical properties are presented in **Figure 4**. The bulk sample (Figure 4a) of Mn_2SnO_4 shows an absorption edge around 2 eV, whereas the thin-film sample (Figure 4b) of Mn_2SnO_4 shows a rather slow and continuous absorption onset between 2 and 3 eV (calculated at 2.7 eV). The calculated spectra (Figure 4c) show also the slow onset of absorption in Mn_2SnO_4, which is due to the direct, but dipole-forbidden nature of the band-gap.

The bulk sample of Cr_2MnO_4 (Figure 4a) shows an absorption edge at 3.4–3.5 eV. The calculated band gap edge of Cr_2MnO_4 is slightly indirect, but strong absorption occurs at energies just above the band gap around 3.5 eV (Figure 4c). There are also sub-gap absorption bands around 2.1 and 2.8 eV, which can be attributed to internal d–d transitions of Cr that occur at identical energies in Cr_2O_3.[37] The Cr_2MnO_4 thin-film exhibits sub-gap features starting around 2.5 eV (Figure 4b). The strength of this sub-gap absorption depends on the growth conditions (less absorption at lower pO_2), and is tentatively associated with Mn(III) due to Mn_{Cr} antisite defects. Indeed, our GW calculations for the related Mn(III)-containing compounds Mn_2CrO_4 and Mn_3O_4 show that the empty *d*-states of Mn(III) cause a lowering of the band gap and absorption threshold to energies around 2.5 eV. The internal d–d transitions observed in the bulk samples are sufficiently weak so that they do not cause significant absorption in the thin-film form. Note that the calculated spectrum does not include the Cr internal d–d transitions. Such d–d transitions, known to be strong in some of the open-shell 3*d* compounds led to the commonly accepted view that no open-shell transition-metal-oxides should be considered for TCO applications.[13,41] However, considering the absorption strength, both materials here can be considered as reasonably transparent for most TCO applications. For example, the absorption coefficient of about 2×10^4 cm^{-1} at sub-gap energies in Cr_2MnO_4 corresponds to 80% transmission for a film thickness of 100 nm.

4.3. Electrical Properties of Undoped Candidates

Conductivity measurements were performed for the best-of-class materials Mn_2SnO_4 and Cr_2MnO_4. In the case of thin films, we attempted conductivity measurements using a collinear 4-point probe setup with 1.3 mm distance between the spring-loaded probes. For bulk pellets, each face was painted with Pelco Colloidal Silver Paste (Ted Pella, Inc., Redding, CA). The painted electrodes were then cured at 120 °C for 1–2 h. AC impedance spectroscopy using a custom-built spring-loaded sample holder and a HP 4192A analyzer (Agilent Technologies, Santa Clara, CA) was used to measure the total resistances of the samples, which were then converted to conductivity values by correcting for geometry.

The conductivity of the undoped thin films was too small to be measured, and only the upper bound on the conductivity was estimated to be 10^{-3} S cm^{-1}. The bulk samples had conductivities of less than 10^{-8} S cm^{-1}. Thus, both materials show an insulating behavior. As discussed before, the insulating behavior of Cr_2MnO_4 should result from its DT-4 character, where hole-producer defects are absent. The insulating behavior in Mn_2SnO_4 could be related to the actual growth condition that was perhaps not Mn-rich, or due to the self-trapping behavior of holes that could explain the low conductivity by a small-polaron conduction mechanism, even with the presence of carriers. Therefore, we will now address the tendency for hole self-trapping in these two materials.

4.4. Tendency of Hole Self-Trapping (M-4)

The standard density functional theory (DFT) method within local density approximation (LDA) or semi-local generalized gradient approximation (GGA) generally favors delocalized solutions for electron or hole carriers,[42] and hence, cannot correctly describe a locally distorted structure of a polaronic state, where a hole is localized on a specific atomic site. Since this delocalization bias is not generally removed by improved functionals like DFT+U[30] or computationally more expensive hybrid-functionals,[43] we applied the generalized Koopmans approach[44,45] to restore the physically correct behavior. The

Table 2. The calculated thermal ionization energies for the acceptors formed by substitution of monovalent cations (Li, Na, K, Rb, Cu, Ag) for Mn(II), and of divalent cations (Mg, Zn) for Cr(III). Values in parenthesis include the deepening of the acceptor level due to polaronic localization.

Dopant	Li_{Mn}	Na_{Mn}	K_{Mn}	Rb_{Mn}	Cu_{Mn}	Ag_{Mn}	Mg_{Cr}	Zn_{Cr}
$\varepsilon(0/-1)$ [eV]	0.2 (0.2)	0.2 (0.3)	0.3 (0.5)	0.4	1.0	0.4	0.3 (0.4)	0.3 (0.5)

generalized Koopmans approach removes the (de)localization bias by means of a so-called hole-state potential (applied to those orbitals that can self-trap carriers, e.g. Mn-*d*), and allows the quantitative calculation of the self-trapping energy E_{ST}. It has recently been employed in the prototypical binary d^5 systems MnO and Fe_2O_3.[16]

For Mn_2SnO_4 and Cr_2MnO_4, we first considered the tendency of Mn^{+II} ions to self-trap holes by forming Mn^{+III} polarons. A negative self-trapping energy of –0.6 eV is found for the octahedrally coordinated Mn site in Mn_2SnO_4, indicating that the experimental marginal conductivity of this material originates from a small-polaron conduction mechanism. Consequently, Mn_2SnO_4 was ultimately discarded as a candidate TCO material (see Figure 1). The tetrahedrally coordinated Mn-site shows positive trapping energies of E_{ST} = +1.0 and +0.5 eV in Mn_2SnO_4 and Cr_2MnO_4, respectively. This finding correlates well with our recent study on the binary MnO, where we found self-trapping for Mn_{Oh} in the rock-salt structure, but not for Mn_{Td} in the (metastable) zinc-blende structure.[16] Thus, the present study corroborates the preference of tetrahedral over octahedral Mn coordination, which can serve as a new design principle for selecting initial pool of materials in future studies.

The possibility that a Cr^{+IV} polaron could form in Cr_2MnO_4 was also considered, but it was found to be unstable. Thus, Cr_2MnO_4 is the remaining candidate material that satisfies all desired intrinsic materials properties (Figure 1b).

4.5. Extrinsic Defect Properties: Suitable Acceptor Dopants as Hole Producers in Cr_2MnO_4 (M-6)

In the preceding steps, Cr_2MnO_4 was identified as a thermodynamically stable, acceptably transparent (as thin-film), and p-type dopable oxide, which unlike many other transition-metal oxides does not self-trap hole-carriers. The absence of an intrinsic hole-producing defect due to the "doping-type 4" behavior (no net hole killers but no net hole producers either), however, requires searching for a suitable dopant to achieve significant p-type conductivity. In this regard, Cr_2MnO_4 is not different than common n-type TCOs, where the desired conductivities are achieved through extrinsic doping, for example, in ZnO:Al,[46] or In_2O_3:Sn.[47] Next, we will address the solubility and acceptor ionization energies of possible dopant atoms, that is, monovalent substitution for Mn(II) and divalent substitution for Cr(III).

4.5.1. Theory of Extrinsic Doping in Cr_2MnO_4 (M-6)

The monovalent and divalent elements Li, Na, K, Rb, Cu, Ag, Mg, and Zn were considered as the external dopants, and their defect formation energies and transition energy levels were calculated for the substitutional impurities on both the Cr and Mn sites. Donor configurations like Li interstitials,[48,49] which could form due to the small ionic size of Li, have also been considered explicitly, but these were found to have sufficiently high formation energies so as not to compensate p-type doping.

In **Table 2**, the calculated acceptor ionization energies for the acceptor defects from the extrinsic doping are listed. Among these defects, Li_{Mn}, Na_{Mn}, K_{Mn}, Mg_{Cr}, and Zn_{Cr} have small acceptor ionization energies. For these defects, the stability of the defect-bound oxygen polaron (O^{-I}) was also tested, using the Koopmans condition approach mentioned above,[44] and the corresponding acceptor ionization energies are also shown in Table 2. Since polaronic localization generally causes the acceptor ionization energy to increase, we discard all acceptors with levels that are already rather deep (Rb, Cu, Ag). The remaining five acceptors show indeed a tendency to form a defect-bound oxygen polaron (O^{-I}), which results in an increase of the ionization energy from 0.3 eV to 0.5 eV for K_{Mg} and Zn_{Cr}, from 0.3 eV to 0.4 eV for Mg_{Cr} and from 0.2 eV to 0.3 eV for Na_{Mn}. In the case of the Li_{Mn} acceptor, the ionization energy is only marginally increased due to the polaronic localization, which is similar to the case of Mg_{Ga} in GaN.[50]

In order to determine the solubility limits of extrinsic dopants, growth under equilibrium conditions was considered, where the chemical potentials of all elements are constrained by the requirement that the host Cr_2MnO_4 is thermodynamically stable with respect to decomposition into the elements, and binary or other ternary compounds, including for example, Cr_2O_3, Mn_2CrO_4, $LiCrO_2$, $MgCr_2O_4$, and Mg_6MnO_8. The defect concentration and the free charge carrier concentration can be obtained as a function of growth temperature, T_g, and oxygen partial pressure, pO_2, from a thermodynamic model,[6,23] where the Fermi level, defect formation energy, and the concentration of defects and free charge carriers were numerically calculated in a self-consistent way under the constraint of overall charge neutrality.

In **Figure 5**a,b, the calculated solubility limit of hole producer (Li_{Mn} or Mg_{Cr}), and hole carriers at room temperature

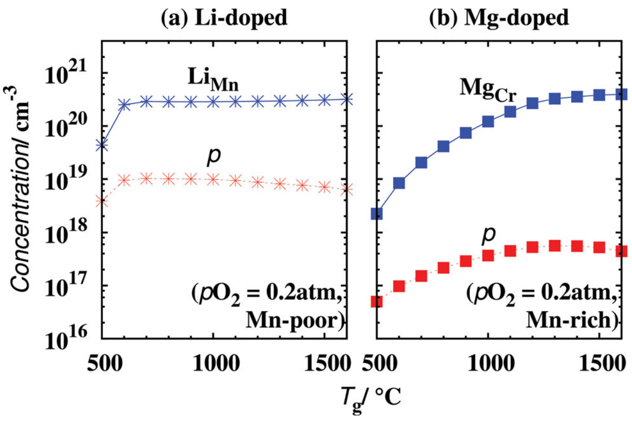

Figure 5. The calculated solubility limit of the hole producer (Li_{Mn} or Mg_{Cr}) and hole carrier concentration at room temperature in a) Li-doped and b) Mg-doped Cr_2MnO_4, as a function of the growth temperature (T_g).

are shown as a function of the growth temperature for Li- and Mg-doped Cr_2MnO_4. The oxygen partial pressure is taken as $pO_2 = 0.2$ atm, corresponding to that in air, while the Mn-poor and Mn-rich conditions are employed to facilitate the formation of Li_{Mn} and Mg_{Cr} for Li- and Mg-doped samples respectively. As shown in Figure 5a, the solubility limit of Li_{Mn} is consistently around 3×10^{20} cm^{-3}, which is about 0.8 cat% (cation percent), when the growth temperature is above 600 °C. The corresponding hole carrier concentration at room temperature is on the order of 10^{19} cm^{-3}. The hole carrier concentration in the Mg-doped Cr_2MnO_4 stays considerably below that of the Li-doped case, mainly due to the larger ionization energy of Mg_{Cr}. However the maximum of $p = 6 \times 10^{17}$ cm^{-3} is still comparable with the typical value in most p-type wide-gap materials such as $CuAlO_2$ (1.3×10^{17} cm^{-3}),[11] ZnO:Li ($1.44–6.04 \times 10^{17}$ cm^{-3}),[49,51] and GaN:Mg ($0.7–2.03 \times 10^{17}$ cm^{-3}).[52]

In practice, the solubility limit could be overcome using low-temperature non-equilibrium processes, since phase separation often requires high temperature and long diffusion time. For example, the solid solubility of Sn in In_2O_3 is about 3 cat% in the temperature range from 900 to 1375 °C,[53] but thin-films with up to 40 cat% Sn in solution can be obtained in phase-pure bixbyite.[54] Besides the ability to exceed the thermodynamic solubility limit, non-equilibrium growth can also increase the disorder of the cation-distribution in ternary oxides.[7] This effect could be important for Mg-doping of Cr_2MnO_4, since we find that the electrically inactive Mg_{Mn} defect has lower formation energy than the acceptor-like defect Mg_{Cr}, so that the doping efficiency of Mg would be rather low when the site-occupancy of Mg is allowed to equilibrate. Taking into account the potential enhancement of p-type doping due to non-equilibrium effects, **Figure 6** shows the calculated hole carrier concentration at room temperature as a function of the concentration of Li_{Mn} or Mg_{Cr} acceptors beyond the equilibrium limits. We found at the same defect concentration, the free hole carrier concentration in Mg-doped sample is always about one order of magnitude less than Li-doped sample, which is due to the higher thermal ionization energy of Mg_{Cr} than Li_{Mn} (0.4 eV vs. 0.2 eV after including the effect of the defect-bound polaron, see Table 2).

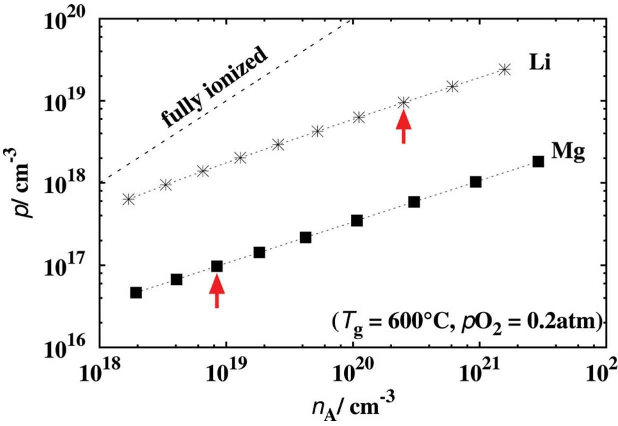

Figure 6. The calculated free hole carrier concentration at room temperature as a function of acceptor defect (hole producer) concentration in Li- and Mg-doped Cr_2MnO_4. The arrows denote the solubility limit from equilibrium growth in air ($pO_2 = 0.2$ atm) at $T_g \geq 600$ °C.

We find that carrier concentrations above 10^{19} cm^{-3} and 10^{18} cm^{-3} should be possible with Li and Mg doping, respectively.

4.5.2. Preliminary Synthesis of Li-Doped Cr_2MnO_4

Theoretical calculations suggest that lithium prefers to occupy the tetrahedral (Mn) site in the spinel crystal structure. Several bulk samples with different lithium concentrations were therefore synthesized via substituting Li for Mn in a 1:1 ratio. Although the results are preliminary, lithium doping has increased the p-type conductivity in bulk Cr_2MnO_4 by several orders of magnitude. The maximum conductivity achieved was 1.1×10^{-2} S cm^{-1}, approaching the conductivities observed in prototypical p-type TCOs like $CuAlO_2$.[11,55] Ongoing studies will address the potential of thin-film growth to exploit the non-equilibrium effects described above, and bulk studies are being conducted to confirm the predicted solubility limit.

5. Conclusions

In this study, we illustrate the complete workflow of the Inverse Design approach as applied to the search for novel p-type transparent oxides. Based on a design principle that suggests the use of high-spin d^5 cations to introduce p–d interaction near the valence band maximum (VBM), we selected 13 ternary Mn oxides from the Inorganic Crystal Structure Database (ICSD), which were narrowed down to the "best-of-class" by high-throughput screening, accounting for the multi-targeted nature of the desired materials properties. We have then performed initial materials synthesis and a more detailed experimental and theoretical study, which resulted in the identification of Cr_2MnO_4 as a thermodynamically stable, wide-gap, and p-type dopable oxide without hole-carrier self-trapping, otherwise a common obstacle for p-type conduction in transition metal oxides. Lacking an intrinsic hole-producing acceptor-type defect, Cr_2MnO_4 requires extrinsic impurity doping. We identified Li as a suitable acceptor-dopant, and initial synthesis of such doped samples was shown to enhance the conductivity by five orders of magnitude. The present study exemplifies the Inverse Design approach for identifying compounds with desired target properties.

Acknowledgements

This work was supported by the U.S. Department of Energy, Office of Science, Office of Basic Energy Sciences, Energy Frontier Research Centers, under Contract No. DE-AC36-08GO28308 to NREL. The high performance computing resources of the National Energy Research Scientific Computing Center and of NREL's Computational Science Center are gratefully acknowledged. This work made use of the J. B. Cohen X-Ray Diffraction Facility supported by the MRSEC program of the National Science Foundation (DMR-1121262) at the Materials Research Center of Northwestern University.

Received: March 5, 2013

[1] J. Tate, D. A. Keszler, in *Transparent electronics: from synthesis to applications*, (Eds: A. Facchetti, T. J. Marks), John Wiley and Sons Ltd., Chichester, UK **2010**.
[2] a) S. Pearton, D. P. Norton, K. Ip, Y. W. Heo, T. Steiner, *Progress in Materials Science* **2005**, *50*, 293; b) C. Klingshirn, *Chem Phys Chem* **2007**, *8*, 782; c) M. D. McCluskey, S. J. Jokela, *J. Appl. Phys.* **2009**, *106*, 071101; d) A. Janotti, C. G. Van de Walle, *Rep. Prog. Phys.* **2009**, *72*, 126501.
[3] A. Franceschetti, A. Zunger, *Nature* **1999**, *402*, 60.
[4] a) S. V. Dudiy, A. Zunger, *Phys. Rev. Lett.* **2006**, *97*, 046401; b) P. Piquini, P. A. Graf, A. Zunger, *Phys. Rev. Lett.* **2008**, *100*, 186403; c) M. d'Avezac, J.-W. Luo, T. Chanier, A. Zunger, *Phys. Rev. Lett.* **2012**, *108*, 027401.
[5] a) G. Bergerhoff, I. D. Brown, *Crystallographic Databases* International Union of Crystallography, Chester, UK **1987**; b) A. Belsky, M. Hellenbrandt, V. L. Karen, P. Luksch, *Acta Cryst.* **2002**, *B58*, 364.
[6] G. Trimarchi, H. Peng, J. Im, A. Freeman, V. Cloet, A. Raw, K. Poeppelmeier, K. Biswas, S. Lany, A. Zunger, *Phys. Rev. B* **2011**, *84*, 165116.
[7] J. Perkins, T. Paudel, a. Zakutayev, P. Ndione, P. Parilla, D. Young, S. Lany, D. Ginley, a. Zunger, N. Perry, Y. Tang, M. Grayson, T. Mason, J. Bettinger, Y. Shi, M. Toney, *Phys. Rev. B* **2011**, *84*, 205207.
[8] L. Yu, A. Zunger, *Phys. Rev. Lett.* **2012**, *108*, 068701.
[9] X. Zhang, L. Yu, A. Zakutayev, A. Zunger, *Adv. Funct. Mater.* **2012**, *22*, 1425.
[10] X. Zhang, V. Stevanovi , M. d'Avezac, S. Lany, A. Zunger, *Phys. Rev. B* **2012**, *86*, 014109.
[11] H. Kawazoe, M. Yasukawa, H. Hyodo, M. Kurita, H. Yanagi, H. Hosono, *Nature* **1997**, *389*, 939.
[12] A. R. Nagaraja, N. H. Perry, T. O. Mason, Y. Tang, M. Grayson, T. R. Paudel, S. Lany, A. Zunger, *J. Am. Ceram. Soc.* **2012**, *95*, 269.
[13] H. Kawazoe, H. Yanagi, K. Ueda, H. Hosono, *MRS Bull.* **2000**, *25*, 28.
[14] S. H. Song, Z. X. Yuan, P. Xiao, *J. Mater. Sci. Lett.* **2003**, *22*, 755.
[15] a) Z. Lu, J. Zhu, E. Andrew Payzant, M. P. Paranthaman, *J. Am. Ceram. Soc.* **2005**, *88*, 1050; b) W. Qu, L. Jian, J. M. Hill, D. G. Ivey, *J. Power Sources* **2006**, *153*, 114.
[16] H. Peng, S. Lany, *Phys. Rev. B* **2012**, *85*, 201201.
[17] D. O. Scanlon, K. G. Godinho, B. J. Morgan, G. W. Watson, *J. Chem. Phys.* **2010**, *132*, 024707.
[18] a) H. Raebiger, S. Lany, A. Zunger, *Phys. Rev. B* **2007**, *76*, 045209; b) X. Nie, S.-H. Wei, S. Zhang, *Phys. Rev. Lett.* **2002**, *88*, 066405.
[19] a) A. J. Boman, H. J. van Daal, *Adv. Phys.* **1970**, *19*; b) A. M. Stoneham, J. Gavartin, A. L. Shluger, A. V. Kimmel, D. Muñoz Ramo, H. M. Rønnow, G. Aeppli, C. Renner, *J. Phys.: Condens. Matter* **2007**, *19*, 255208.
[20] B. J. Ingram, T. O. Mason, R. Asahi, K. T. Park, A. J. Freeman, *Phys. Rev. B* **2001**, *64*, 155114.
[21] S. Lany, A. Zunger, *Phys. Rev. B* **2008**, *78*, 235104.
[22] A. Zunger, *Appl. Phys. Lett.* **2003**, *83*, 57.
[23] S. Lany, A. Zunger, *Phys. Rev. Lett.* **2007**, *98*, 045501.
[24] S. Lany, J. Osorio-Guillén, A. Zunger, *Phys. Rev. B* **2007**, *75*, 241203.
[25] G. Mandel, *Phys. Rev.* **1964**, *134*, A1073.
[26] T. R. Paudel, A. Zakutayev, S. Lany, M. d'Avezac, A. Zunger, M. Avezac, *Adv. Funct. Mater.* **2011**, *21*, 4493.
[27] a) P. E. Blöchl, *Phys. Rev. B* **1994**, *50*, 17953; b) G. Kresse, D. Joubert, *Phys. Rev. B* **1999**, *59*, 1758.
[28] a) G. Kresse, J. Hafner, *Phys. Rev. B* **1993**, *47*, 558; b) G. Kresse, J. Hafner, *Phys. Rev. B* **1994**, *49*, 14251; c) M. Shishkin, G. Kresse, *Phys. Rev. B* **2006**, *74*, 035101.
[29] J. P. Perdew, K. Burke, M. Ernzerhof, *Phys. Rev. Lett.* **1996**, *77*, 3865.
[30] S. L. Dudarev, G. A. Botton, S. Y. Savrasov, C. J. Humphreys, A. P. Sutton, *Phys. Rev. B* **1998**, *57*, 1505.
[31] V. Stevanović, S. Lany, X. Zhang, A. Zunger, *Phys. Rev. B* **2012**, *85*, 115104.
[32] L. Hedin, *Phys. Rev.* **1965**, *139*, A796.
[33] J. Osorio-Guillén, S. Lany, S. Barabash, A. Zunger, *Phys. Rev. Lett.* **2006**, *96*, 107203.
[34] J. Paier, M. Marsman, G. Kresse, *Phys. Rev. B* **2008**, *78*, 121201.
[35] S. Lany, *Phys. Rev. B* **2013**, *87*, 085112.
[36] M. Tabbal, S. Kahwaji, T. C. Christidis, B. Nsouli, K. Zahraman, *Thin Solid Films* **2006**, *515*, 1976.
[37] C.-S. Cheng, H. Gomi, H. Sakata, *Phys. Status Solidi A* **1996**, *155*, 417.
[38] H. J. Monkhorst, J. D. Pack, *Phys. Rev. B* **1976**, *13*, 5188.
[39] a) R. D. Shannon, J. L. Gillson, R. J. Bouchard, *J. Phys. Chem. Solids* **1977**, *38*, 877; b) B. J. Ingram, G. B. Gonzalez, D. R. Kammler, M. I. Bertoni, T. O. Mason, *J. Electroceram.* **2004**, *13*, 167.
[40] P. Kubelka, F. Munk, *Z. Techn. Phys.* **1931**, *12*, 12593.
[41] D. A. Keszler, K. R. Poppelmeier, unpublished.
[42] J. Lægsgaard, K. Stokbro, *Phys. Rev. Lett.* **2001**, *86*, 2834.
[43] a) J. Heyd, G. E. Scuseria, M. Ernzerhof, *J. Chem. Phys.* **2003**, *118*, 8207; b) J. Heyd, G. E. Scuseria, *J. Chem. Phys.* **2004**, *121*, 1187; c) J. Paier, M. Marsman, K. Hummer, G. Kresse, I. C. Gerber, J. G. Angyan, *J. Chem. Phys.* **2006**, *124*, 154709; d) J. Paier, M. Marsman, K. Hummer, G. Kresse, I. C. Gerber, J. G. Angyan, *J. Chem. Phys.* **2006**, *125*, 249901.
[44] S. Lany, A. Zunger, *Phys. Rev. B* **2009**, *80*, 085202.
[45] S. Lany, *Phys. Status Solidi B* **2011**, *248*, 1052.
[46] C. Klingshirn, *Phys. Status Solidi B* **2007**, *244*, 3027.
[47] a) G. Frank, H. Köstlin, *Appl. Phys. A* **1982**, *27*, 197; b) G. B. Gonzalez, T. O. Mason, J. P. Quintana, O. Warschkow, D. E. Ellis, J. H. Hwang, J. P. Hodges, J. D. Jorgensen, *J. Appl. Phys.* **2004**, *96*, 3912.
[48] X. H. Wang, B. Yao, Z. Z. Zhang, B. H. Li, Z. P. Wei, D. Z. Shen, Y. M. Lu, X. W. Fan, *Semicond. Sci. Technol.* **2006**, *21*, 494.
[49] J. G. Lu, Y. Z. Zhang, Z. Z. Ye, Y. J. Zeng, H. P. He, L. P. Zhu, J. Y. Huang, L. Wang, J. Yuan, B. H. Zhao, X. H. Li, *Appl. Phys. Lett.* **2006**, *89*, 112113.
[50] S. Lany, A. Zunger, *Appl. Phys. Lett.* **2010**, *96*, 142114.
[51] Y. J. Zeng, Z. Z. Ye, W. Z. Xu, D. Y. Li, J. G. Lu, L. P. Zhu, B. H. Zhao, *Appl. Phys. Lett.* **2006**, *88*, 062107.
[52] a) U. Kaufmann, P. Schlotter, H. Obloh, K. Köhler, M. Maier, *Phys. Rev. B* **2000**, *62*, 10867; b) A. K. Rice, K. J. Malloy, *J. Appl. Phys.* **2001**, *89*, 2816.
[53] G. B. González, T. O. Mason, J. S. Okasinski, T. Buslaps, V. Honkimäki, *J. Am. Ceram. Soc.* **2012**, *95*, 809.
[54] P. Parent, H. Dexpert, G. Tourillon, J. M. Grimal, *J. Electrochem. Soc.* **1992**, *139*, 276.
[55] J. Tate, H. Ju, J. Moon, A. Zakutayev, A. Richard, J. Russell, D. McIntyre, *Phys. Rev. B* **2009**, *80*, 165206.